
Article:
Gaspar, H., Teixeira, P., Bernardo, C. et al. (13 more authors) (2017) A journey along the extruder with polystyrene:C60 nanocomposites: convergence of feeding formulations into a similar nanomorphology. Macromolecules, 50 (8). pp. 3301-3312. ISSN 0024-9297

https://doi.org/10.1021/acs.macromol.6b02283

A Journey Along the Extruder with Polystyrene:C60 Nanocomposites: Convergence of Feeding Formulations into a Similar Nano-Morphology

Journal:	*Macromolecules*
Manuscript ID	ma-2016-02283g.R2
Manuscript Type:	Article
Date Submitted by the Author:	n/a
Complete List of Authors:	Gaspar, Hugo; Universidade do Minho Instituto de Polimeros e Compositos Teixeira, Paulo; Universidade do Minho Instituto de Polimeros e Compositos Santos, Raquel; University of Minho, Fernandes, Liliana; Universidade do Minho Instituto de Polimeros e Compositos Hilliou, Loic; I3N-Institute for Nanostructures, Nanomodelling and Nanofabrication, Department of Polymer Engineering Weir, Michael; The University of Sheffield, Department of Physics and Astronomy Parnell, Andrew; The University of Sheffield, Department of Physics and Astronomy Abrams, Kerry; The University of Sheffield Hill, Christopher; The University of Sheffield Bouwman, Wim; TU Delft, Department of Radiation, Radionuclides & Reactors Parnell, Steven; Delft University of Technology, Faculty of Applied Sciences; Indiana University, Center for Exploration of Energy and Matter King, Stephen; ISIS Pulsed Neutron and Muon Source, Clarke, Nigel; University of Sheffield, Department of Physics and Astronomy Covas, José; Institut for Polymers and Composites, Dept. of Polymer Engineering, University of Minho Bernardo, Gabriel; University of Sheffield, Physics and Astronomy

A Journey Along the Extruder with Polystyrene:C_{60} Nanocomposites: Convergence of Feeding Formulations into a Similar Nano-Morphology

Hugo Gaspar[1], Paulo Teixeira[1], Raquel Santos[1], Liliana Fernandes[1], Loic Hilliou[1], Michael P. Weir[2], Andrew J. Parnell[2], Kerry J. Abrams[3], Christopher J. Hill[4], Wim G. Bouwman[5], Steven R. Parnell[5], Stephen M. King[6], Nigel Clarke[2], José A. Covas[1,*], Gabriel Bernardo[1,*,ψ]

[1]Institute for Polymers and Composites/I3N, University of Minho, 4800-058 Guimarães, Portugal

[2]Department of Physics and Astronomy, The University of Sheffield, Sheffield S3 7RH, United Kingdom

[3]Department of Materials Science and Engineering, The University of Sheffield, Sheffield S1 3JD, United Kingdom

[4]Department of Biomedical Science, The University of Sheffield, Sheffield S3 7HF, United Kingdom

[5]Faculty of Applied Sciences, Delft University of Technology, Mekelweg 15, 2629 JB Delft, Netherlands

[6]ISIS Pulsed Neutron Source, STFC Rutherford Appleton Laboratory, Harwell Campus, Didcot, OX11 0QX, United Kingdom

*Corresponding authors: gabriel.bernardo@dep.uminho.pt; jcovas@dep.uminho.pt

[ψ]Present address: Department of Physics and Astronomy, The University of Sheffield, Sheffield S3 7RH, United Kingdom

Abstract

In this work we investigated the effect of the feeding formulation (pre-mixed powders of pure components versus solvent-blended mixture) of polystyrene-C_{60} composites on the dispersion and re-agglomeration phenomena developing along the barrel of a twin screw extruder. The dispersion of C_{60} in the PS matrix is studied over different length-scales using a combination of optical microscopy, Spin-Echo-Small Angle Neutron Scattering (SESANS), Small Angle Neutron Scattering (SANS), Small Angle X-ray Scattering (SAXS) and Wide Angle X-ray Scattering (WAXS). When a solvent-blended mixture is used as the feeding formulation, the inlet material contains essentially molecularly dispersed C_{60} as revealed by the nano-domains with very small phase contrast. However, C_{60} re-agglomeration occurs along the extruder, creating a morphology still containing only nano-domains but with much higher phase contrast. In the case of mixed powders, the material evolves from the initial macroscopic mixture of pure polystyrene and C_{60} into a composite simultaneously containing micro- and nano-aggregates of C_{60} as well as C_{60} molecularly dispersed in the matrix. Our results show that the two different initial feeding formulations with widely different initial morphologies converge along the extruder, through opposite morphological pathways, into a similar final nanomorphology which is dictated by the interplay between the thermodynamics of the system and the flow. Correlations between the morphological evolution along the extruder and the thermo-rheological properties of the composites are identified.

Keywords: Nanocomposites; Small Angle Neutron Scattering (SANS); Spin-Echo-SANS (SESANS); Small Angle X-ray Scattering (SAXS); fullerene C_{60}; extrusion

1. Introduction

Polymer nanocomposites containing carbon nanoparticles such as graphenes [1, 2], carbon nanotubes [3-7] and fullerenes [8] open a new horizon for polymeric-based materials. These materials benefit from a synergistic combination of useful polymer properties, such as low density, flexibility, ease of processing and cost efficiency, with nanoparticles that not only significantly enhance the mechanical, electrical, and thermal properties of the resulting composite [9], as well as create novel functionalities. Although the homogeneous dispersion and distribution of carbon nanoparticles in a polymer matrix is generally desired to maximize performance, some level of particle aggregation can be advantageous in specific applications [10, 11]. Though property improvements have been achieved in a variety of nanocomposites, carbon nanoparticle dispersion remains difficult to control, with both thermodynamic and kinetic processes playing significant roles.

The dispersion of carbon nanotubes and graphenes is complicated by their strong van der Waals interactions, chemical inertia that creates weak interfaces with most polymers, as well as difficulty to control initial size and shape of these nanoparticles. These parameters influence the cohesiveness of the agglomerates and have been related to dispersion routes such as rupture and erosion [12, 13]. Conversely, fullerene C_{60} (also known as buckminsterfullerene) has a very well defined size and shape: it is a bucky-ball with a diameter of 0.7 nm [14, 15]. When replacing graphenes or carbon nanotubes by fullerenes in a polymer composite, particle size and geometry change (these being associated with entropic changes) while the differences in enthalphic interactions between the particles and the matrix are kept at a minimum. For this reason, polymer composites with C_{60} can be used as model systems to help understand the dispersion of carbon nanoparticles.

In the last two decades, polystyrene (PS) composites containing fullerene nanoparticles have been the subject of a number of studies [15-33] reporting improvements in properties such as electrical conductivity [22, 23], thermal stability [24-27] and permeability [28, 29]. The impact of C_{60} loading and sample preparation conditions on the corresponding glass transition temperature (T_g) and melt viscosity, has also received attention [16, 19, 34].

Campbell et al [21] used wide-angle X-ray scattering (WAXS) to determine the miscibility limit of C_{60} in PS as being ~1 wt%. In this context miscibility is understood as an absolute thermodynamic value associated with molecular homogeneity and which is reversible and independent of the pathway followed from aggregates to molecular dispersion, i.e. it is a maximum value that is independent of processing. An identical miscibility threshold was determined by Sanz et al [34], using a combination of microscopy, SANS and WAXS experiments. Additionally, these authors also determined a dispersibility threshold of ~4 wt% C_{60}, where this is the maximum C_{60} loading associated with the maximum observed increase in the T_g of the composites. Loadings beyond this concentration gradually reverted the composite T_g towards the neat PS value. Increases in T_g with C_{60} loadings in PS composites were also reported by Weng et al [32] and by Wong et al [19], with the latter also concluding that beyond 1 wt% nanoparticle concentration, the C_{60} is aggregated in polydispersed aggregates. Self-assembly of C_{60} into clusters within PS-C_{60} thin films was also reported, with the size of the clusters becoming macroscopic for C_{60} concentrations in the range 3 wt% – 4 wt% C_{60} [30].

The impact of C_{60} on the melt viscosity of PS-C_{60} composites was studied by Tuteja et al [16]. They showed that a viscosity reduction in the PS-C_{60} nanocomposites may occur if the polymer is entangled ($M > M_c$, where M_c is the critical molecular mass critical mass for entanglement coupling) and if the average interparticle half-gap (h) is less than the polymer size (i.e. $h < R_g$), where $h/a = [\Phi_m/\Phi]^{1/3} - 1$, Φ_m being the maximum random packing volume fraction (~0.638) and a being the particle radius (~0.4 nm). For non-entangled polymer melts

($M < M_c$), a viscosity increase is observed upon the addition of C_{60}. In practice, the authors observed a viscosity decrease in well dispersed fullerene-polystyrene nanocomposites prepared via rapid precipitation from solution and using a PS with Mw= 393 kDa. On the other hand, a viscosity increase was observed when using a PS with Mw=19.3 kDa.

In most of the preceding studies, PS-C_{60} blending was achieved through the use of solvents, using methods such as solvent casting or rapid precipitation from solution. Despite the fact that in the commodity plastics industry melt extrusion is a ubiquitous process for the manufacturing of polymer nanocomposites, with solvents rarely being used, in the scarce literature studies in which polymer-C_{60} blending was performed in an extruder no attempts were made to assess the dispersion achieved [27]. Therefore, there is an obvious fundamental and practical interest in studying how C_{60} nanoparticles can be mixed with polystyrene in a melt extruder.

In this work, we conduct a detailed investigation of the dispersion of fullerene C_{60} in polystyrene composites along an intermeshing co-rotating twin-screw extruder. We study and compare two different types of melt-processed PS-C_{60} composites that were prepared using identical C_{60} loadings (1 wt%) and processing conditions (flow rate = 130 $g.h^{-1}$, screw speed = 80 rpm; extruder and die set temperature = 200 ºC), but which differ widely on the quality of dispersion of the initial material: (i) mixed powders of pure polystyrene and pure C_{60} and (ii) a solvent pre-processed PS-C_{60} blend. The morphological characterization of the composites was performed using both direct and indirect characterization techniques. Five direct morphological characterization techniques were used to probe four different length-scale regimes, namely: optical microscopy for the ~ 1 mm – 1 μm range; spin-echo small angle neutron scattering (SESANS) [35] for the ~ 20 μm – 200 nm range; small angle neutron scattering (SANS) and small angle x-ray scattering (SAXS) for the ~ 200 nm – 1 nm range and wide angle x-ray scattering (WAXS) for the sub-nanometer range. Additionally, the

composites were characterized by differential scanning calorimetry (DSC) and rheological measurements, as indirect morphological characterization techniques, to provide an overall understanding of the processing-structure-property relationships in these model polymer-fullerene systems.

This paper is organized as follows. We first describe the sample preparation methods. Then we characterize the dispersion of C_{60} in the composite samples using optical microscopy, SESANS, SANS, SAXS and WAXS. Next, we study the variation of the glass transition temperature with sample preparation conditions and we characterize the samples rheologically. Finally, we discuss and rationalize all the results obtained.

2. Experimental Section

2.1 Materials

The C_{60} fullerene used in this work was supplied by Solenne BV (> 99.5% purity, Mw = 720.64 g.mol^{-1} and density = 1.65 g.cm^{-3}). The polystyrene was purchased from Sigma Aldrich (catalog # 430102) with average Mw~192.000, MFI = 6.0-9.0 g/10 min (200°C/5kg) and density of 1.05 g.cm^{-3} at 25 ºC. The polymer R_g is approximately 12 times larger (estimated from $R_g \cong 0.27 M_w^{1/2}$ [36]) than the diameter of C_{60} (~1 nm).

2.2 Nanocomposite preparation

Two different types of PS-C_{60} formulations were prepared as feeding material for the twin screw extruder: (a) 1.0 wt% C_{60} was simply mechanically mixed with PS (hereafter simply referred to as "mixed powders") and (b) mixtures with 1.0 wt% C_{60} were prepared by solution blending followed by co-precipitation in a non-solvent (hereafter referred to as "pre-solvent blended").

In the preparation of the mixed powders formulation, the granulated polystyrene was milled into a fine powder and then thoroughly mixed with the, as purchased, fine C_{60} powder in a rotating mixer.

In the preparation of the pre-solvent blended formulation, appropriate amounts of PS and C_{60} were dissolved in toluene, while stirring at 80 ºC for 4 hours. Then, the solution was added dropwise into a 5-fold volume excess of pre-cooled methanol (T < 0ºC) under continuous stirring, to enable the co-precipitation of the PS-C_{60} composite. The solids were vacuum filtered from methanol using a nylon membrane filter with a pore size of 0.45 μm (Whatman, cat no. 7404-004) and washed with cold methanol. This was followed by drying at ~100 ºC and 10^{-2} mbar for several hours, until no mass changes were detected using a balance with a precision of ±0.01g. Upon drying, light purple fiber composites were obtained. The yield of composite preparation was ~ 100%, showing that no C_{60} and polystyrene losses had occurred. The total amount of pre-solvent blended formulation prepared was ~35 g (after drying). Finally, the fibrous composite was milled into a fine light purple powder.

The two types of feeding formulations were then melt processed in a prototype co-rotating intermeshing twin-screw extruder of modular construction (Figure S.I.1.(a) in Supporting Information), designed to process small amounts of material (in the range of 30-300 g/h) while retaining the same characteristics of larger equipment. The screws have a diameter of 13 mm and an L/D ratio of 27 (Figure S.I.1.(b) in Supporting Information). The screw profile is built by sliding along a shaft conveying (with distinct pitches and lengths) and kneading elements (that can be stacked with variable staggering angles to induce different hydrodynamic stress levels and, therefore, variable balances of distributive/dispersive mixing). The barrel contains nine material sampling ports, evenly distributed along its length. These are manually operated rotary valves which allow one to quickly remove small volumes of material from within the extruder during steady state operation [37, 38]. A miniaturized

prototype volumetric feeder is positioned upstream. The screw profile used in this work contained two kneading zones consisting of four 3 mm thick kneading disks staggered at -30º (for intensive mixing) separated by a conveying zone. The flow channels had a maximum depth of 1.5 mm so that shear rates were relatively high, even at low screw speeds.

Each PS-C_{60} mixture was compounded at a flow rate of 130 g/h, with the screws rotating at 80 rpm. The temperature profile along the barrel and the slit die (5 mm x 1 mm) was kept at a constant 200 ºC for all the processing experiments. In order to track the quality of the mixing along the extruder, spherically-shaped composite samples in their molten state were collected at sampling ports P2 and P9 during steady state extruder operation. These molten samples were then sandwiched between two Teflon sheets placed between two metal plates and slightly compressed, while cooling down to room temperature, into approximately circular disks with thickness ~1.5 mm and diameter ~ 20 mm (see Figure S.I.2 in Supporting Information). These samples, hereafter simply referred to as samples P2 and P9 depending on the sampling port from which they were collected, as well as the extruded ribbons collected after air cooling and winding were then stored for subsequent characterization. To keep the extrusion line running continuously, the lowest possible draw-down (i.e., the ratio between the linear velocity of the winder and the extrudate velocity) was applied.

Additionally, reference samples with C_{60}:PS weight ratios 1:99 were prepared by compression molding: (i) a mixture of the pure powders at 170 ºC and 10 MPa during 5 minutes (1 sample produced); (ii) powders of the solvent blended composite at 90 ºC and 170 ºC and 10 MPa during 5 minutes (2 samples produced). These three reference samples were also stored for subsequent characterization.

All the samples are shown in Figure S.I.2 in Supporting Information. The initial sample compression molded from mixed powders is mostly colourless and transparent, albeit containing a few macroscopic black spots in it. The initial pre-solvent blended sample is

purple and transparent. The samples from mixed powders collected at P2, P9 and ribbon are all dark brown and optically opaque. The samples from pre-solvent blend collected at P2, P9 and ribbon are light brownish and still optically transparent to some degree.

2.3 Nanocomposites characterization

2.3.1. Optical microscopy

The agglomerate size distribution in the initial, i.e. before melt compounding, pre-solvent blended and mixed powder formulations was determined by light transmission optical microscopy (O.M.) using a BH2 Olympus microscope coupled to a Leica DFC 280 camera, with a 1.6 x ocular and 20 x objective magnification. For microscopy observations, the feeding formulations (in powder form) were softened at 160 °C and spread onto a glass slide.

The evolution of dispersion along the extruder was estimated by O.M. For this, 10 µm thin sections were cut from samples at room temperature with a Leitz 1401 microtome using glass knifes with an angle of 45°. The extruded tapes were molded in an epoxy resin and cut perpendicular to the flow direction. Micrographs were acquired using the same microscopy equipment and under similar magnifications. To obtain sufficient statistics, at least six micrographs were analyzed using ImageJ® Software, leading to an investigated total area of 2.1 mm^2.

The level of dispersion was quantified in terms of Area ratio (Ar), which balances the total area of agglomerates and the total area analyzed, and cumulative relative distribution of the agglomerates (C_{C60}). This is determined by summing the areas of the individual agglomerates in ascending area order and dividing by the total area of agglomerates. In particular, the size of the larger agglomerate contained in 75% (Aχ75) and 90% (Aχ90) of the total area of agglomerates were followed.

2.3.2. Spin-Echo Small Angle Neutron Scattering (SESANS)

Spin-Echo Small Angle Neutron Scattering (SESANS) is a relatively new technique to measure structures of materials. Structures can be determined over three orders of magnitude in length scale, from 10 nm to 20 μm. This is two orders of magnitude larger than conventional SANS and comparable to what may be studied with light scattering or OM, though with the complementary benefits afforded by the use of neutrons such as contrast and probing the bulk. However, like O.M., and unlike SANS (or SAXS), SESANS measures in real space.

Briefly, SESANS uses a series of magnetised permalloy films and magnetic fields to encode the scattering angle information in the spin precession of a beam of polarized neutrons. Neutrons scattered through different angles traverse magnetic fields of different lengths and thus precess differently to the unscattered neutrons. The structural length scale probed depends upon the applied magnetic field strength, hence varying the magnetic field strength provides tunability over a range of length scales, termed the spin-echo length.

The SESANS measurements reported here were performed at the Reactor Institute Delft (TU Delft, Netherlands), using a beam monochromatised (using a pyrolytic graphite crystal) to a wavelength λ=2.06 Å [35]. The pre-solvent blend sample was measured for 4 hours whilst the sample from mixed powders was measured for ~12 hours over the same spin-echo length range.

2.3.3. Small Angle Neutron Scattering (SANS)

Small-angle neutron scattering (SANS) measurements were performed at the LOQ diffractometer at the ISIS Pulsed Neutron Source (Rutherford Appleton Laboratory, Oxfordshire, UK) with a polychromatic incident beam of λ = 2 – 10 Å and fixed sample-to-detector distance of 4 m, to provide a scattering vector range of $0.009 < q < 0.25$ Å^{-1}, where

q=(4π/λ)sin(θ/2) and θ is the scattering angle. Due to the high carbon to hydrogen content in C_{60}, there is a naturally high neutron scattering length density contrast with the hydrogenous polystyrene polymer removing the need for isotopic substitution (deuteration). However, there is a greater degree of incoherent background scattering from the matrix that degrades the signal-to-noise, particularly at larger q values.

The samples P2 and P9 were ~ 1.5 mm thick and the extruded ribbons were ~ 0.7 mm thick although their exact thicknesses were measured by a micrometer and those values used in the data reduction procedure to ensure proper intensity scaling. Samples were mounted on a computer-controlled sample changer and SANS patterns were recorded at room temperature for approximately 90 min/sample. Each raw scattering data set was then radially-averaged, corrected for the detector efficiency, sample transmission and background scattering and then converted to scattering cross-section data and plotted on an absolute scale ($\partial\Sigma/\partial\Omega$ vs q) using Mantid software [39]. For convenience, we shall follow the normal convention of referring to $\partial\Sigma/\partial\Omega$ as intensity (I). The corrected data were then fitted to appropriate models using SasView software (Version 3.1.1) [40]. The neutron scattering length densities of hydrogenous PS and of C_{60} are respectively, $\rho_N(H\text{-}PS)$ = 1.41 x 10^{-6} Å^{-2} and $\rho_N(C_{60})$ = 5.60 x 10^{-6} Å^{-2} and therefore $\Delta\rho_N$=4.09 x 10^{-6} Å^{-2}.

2.3.4. Small Angle X-Ray Scattering (SAXS)

SAXS measurements were performed in-house on a Bruker instrument (NanoStar, Department of Chemistry, University of Sheffield, UK) equipped with a microfocus Cu-Kα source (8 keV, λ = 1.54 Å; Xenocs, France), collimating system with motorized scatterless slits (Xenocs, France) and a HiStar 2D multiwire gas detector (Siemens/Bruker). Scattering patterns were corrected for the detector's dark current, spatial distortion, flat field and normalized using sample thickness, exposure time, sample transmission and the detector

normalization coefficient. The electron densities of hydrogenous PS and of C_{60} are respectively, $\rho_{X(H\text{-}PS)}$ = 9.56 x 10^{-6} Å^{-2} and $\rho_{X(C_{60})}$ = 1.40 x 10^{-5} Å^{-2} and therefore $\Delta\rho_X$= 4.44 x 10^{-6} Å^{-2}.

2.3.5. Wide Angle X-Ray Scattering

WAXS measurements, of samples P9 from both mixed powders and solvent processed blend, were performed on a Xeuss 2.0 SAXS/WAXS laboratory beamline using a liquid Gallium MetalJet (Excillum) x-ray source (9.2 keV, λ = 1.34 Å). The scattered X-rays were detected using a Pilatus3R 1M detector. Scattering from the samples was collected at room temperature for 3 minutes.

2.3.6. Differential Scanning Calorimetry

Differential Scanning Calorimetry (DSC) experiments were performed on a Perkin Elmer Pyris-1 calorimeter under nitrogen where temperature and heat capacity were calibrated using a sapphire standard. Thermal history was eliminated by ramping from 25 to 150 ºC at 10 ºC.min^{-1}, isothermal annealing at 150 ºC for 2 minutes, then cooling to 30 ºC at 10ºC.min^{-1}. Two heating-cooling cycles were run. The glass transition temperature T_g was computed from the second heating run following the half-Cp extrapolation method. Error bars in T_g are estimated by the maximum deviation of three independent measurements.

2.3.7. Rheometry

Disks were loaded between the parallel plates (diameter 25 mm) of a stress-controlled rotational rheometer (ARG2, TA Instruments) at a temperature of 200 ºC under air. Time was left for the samples to thermally stabilize and adjust to the defined gap between the parallel plates, as inferred from the on-line reading of the normal force relaxation. A time sweep was first performed at 1 Hz with a deformation of 0.1% (corresponding to the linear regime of

viscoelasticity as inferred from separate strain sweep experiments performed at 1 Hz) to confirm the thermal stability of all samples within 20 minutes. Then a new sample was loaded and equilibrated as mentioned above, for the recording of a mechanical spectrum using a frequency sweep performed with a deformation of 0.1%.

3. Results and Discussion

As an aid to the analysis and discussion of our experimental results, we start by showing in Figure 1 an idealized schematic of the different possible stages of C_{60} dispersion in a polymer matrix.

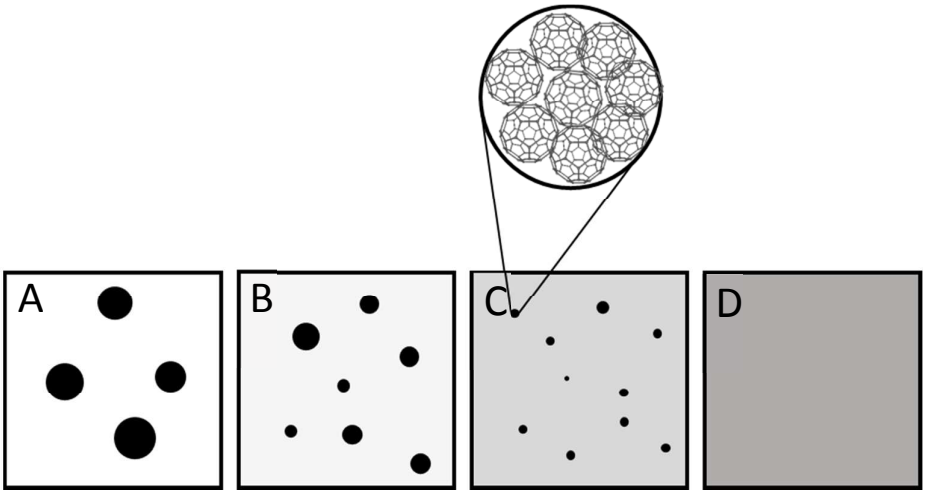

Figure 1. Idealized schematic of C_{60} dispersion in the polymer matrix along the extruder, starting from macroscopic agglomerates of C_{60} in a matrix of pure polymer and ending with an idealized mixture of individual C_{60} molecules homogeneously dispersed in the polymer matrix.

There are two extreme situations, namely situation A in which macroscopic and microscopic agglomerates of C_{60} coexist in a matrix of pure polymer and situation D consisting of an idealized mixture of individual C_{60} molecules homogeneously dispersed in

the polymer matrix. Two intermediate cases (B and C) correspond to a mixture of microscopic and nanoscopic agglomerates of C_{60} in a polymer matrix containing some molecularly dispersed C_{60} and to a mixture of nanoscopic agglomerates in a polymer matrix containing a considerable amount of molecularly dispersed C_{60}, respectively.

The level of dispersion of C_{60} in the initial feeding formulations and in the samples collected along the extruder was first investigated by optical microscopy (O.M.), as shown in Figure 2 and in Figure S.I.3. in Supporting Information.

(a)

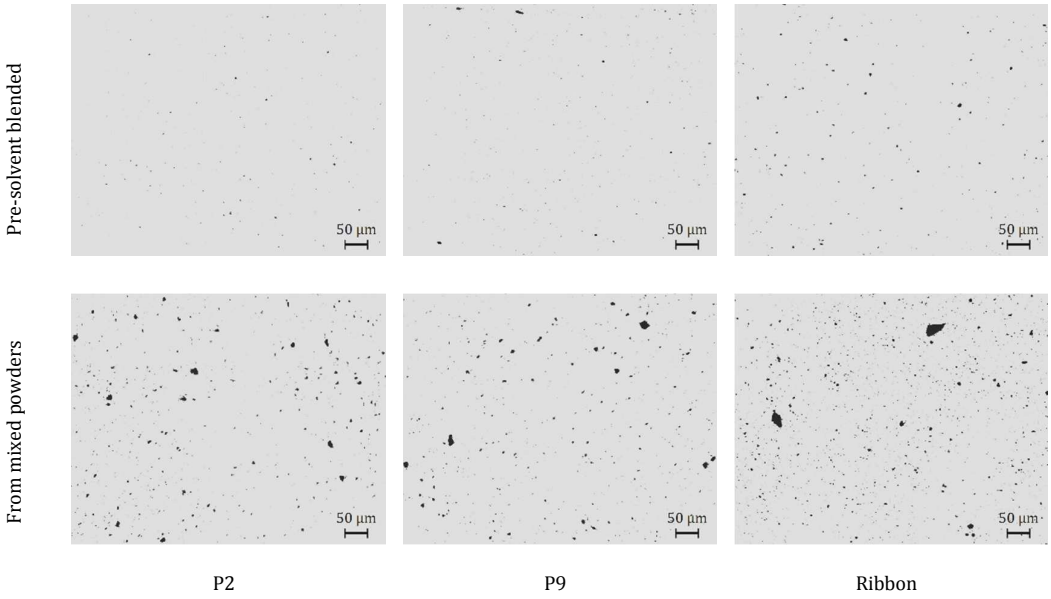

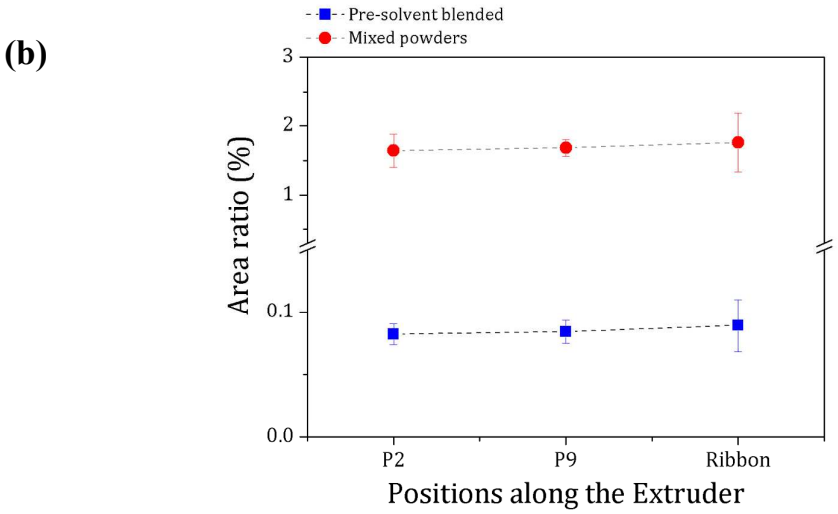

Figure 2. (a) Morphology development of PS nanocomposites containing 1 wt. % of C_{60} along the twin-screw extruder; (b) Area ratio evolution along the twin-screw extruder of PS nanocomposites containing 1 wt. % of C_{60}.

Figure S.I.3. shows optical microscopy images of the initial feeding formulations. The image of the "mixed powders" feeding formulation shows large black aggregates in a matrix of essentially pure polystyrene. Overall this formulation shows both a poor dispersion and poor distribution of the aggregates. By contrast, on the image of the "solvent-blended" feeding formulation, although some randomly distributed darker spots are visible, these are not large black aggregates. These darker spots most likely result from some possible heterogeneities (regions with different PS:C_{60} ratio) inherent to the precipitation process used in the preparation of this composite. Also visible in the "solvent-blended" figure is a larger, approximately circular, feature with ~50 μm diameter which corresponds to material that did not melt during the preparation of the optical microscopy samples.

The morphology development of PS nanocomposites containing 1 wt. % of C_{60} along the extruder is presented in Figure 2(a). As clearly shown, the extruded samples prepared from mixed powders contain a large number of microscopic aggregates. By contrast, in the extruded samples prepared from pre-solvent blend the number and size of microscopic

features is much smaller. Figure 2(b) displays the corresponding evolution of the area ratio and the dispersion characterization results are summarized in Table 1. As shown in Figure 2 and Table 1, in extruded samples from both mixed powders and pre-solvent blend, the area ratio remains approximately constant along the extruder.

It is well accepted that dispersion of solid agglomerates in a molten matrix occurs when the hydrodynamic stresses developed during flow are larger than the cohesive strength of the agglomerates. This balance is usually quantified by the fragmentation number, F_a. It has been suggested that when F_a is large, dispersion is dominated by the rupture of the agglomerates into successively smaller aggregates. When F_a is small, erosion should prevail. This is a much slower dispersion route, whereby small aggregates or individual particles detach from the agglomerates. Both phenomena were reported in studies of the dispersion of carbon nanonotubes and graphite nanoplates [41, 42]. In the present work, as the area ratio remained constant along the extruder, this means that no substantial rupture took place, but some dispersion may have developed via erosion, as in this case the large agglomerates are still visible by optical microscopy.

Position	Pre-solvent blended			From mixed powders		
	$A_{\chi 75\%}$ (μm^2)	$A_{\chi 90\%}$ (μm^2)	N (per mm^2)	$A_{\chi 75\%}$ (μm^2)	$A_{\chi 90\%}$ (μm^2)	N (per mm^2)
P2	16.91	24.07	88 ± 10	59.31	161.88	988 ± 137
P9	17. 48	28.95	88 ± 16	71.34	178.22	980 ± 76
Ribbon	18.86	33.84	92 ± 16	87.43	374.48	1020 ± 235

Table 1. Optical microscopy dispersion characterization results for PS nanocomposites containing 1.0 wt. % of C_{60}

The SESANS data from two nanocomposites extracted from port P9 is shown in Figure 3. The data from the mixed powder sample has been fitted to a model of monodispersed

particles using the Gaussian approximation formalism detailed by Andersson et al [43] and the resulting fit is also shown in Figure 3.

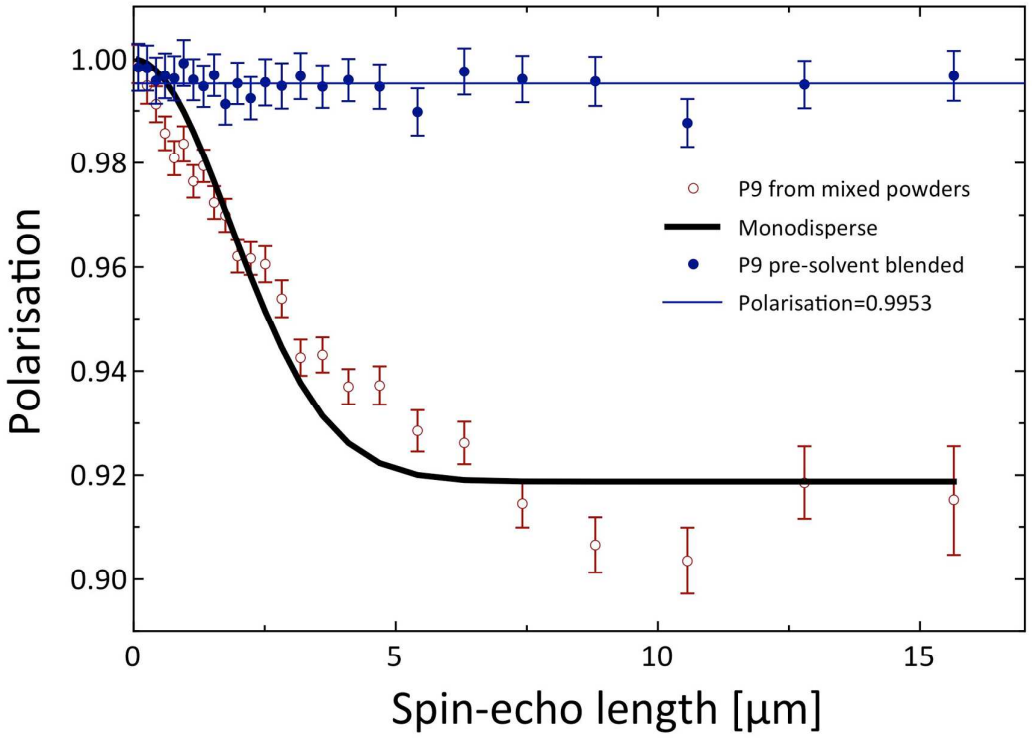

Figure 3. Spin-Echo-SANS signals, expressed as the depolarisation ratio P/P_0, of extruded PS-C_{60} nanocomposites extracted from sampling port #9. The black line is a fit to a monodisperse sphere model whilst the blue line is a constant illustrating a small depolarisation over those length scales probed in the pre-solvent blended sample.

This modelling approach is used as the system is low concentration and no consideration of a structure factor is necessary. The best fit to the data, in which the radius was the only free parameter, was found for particles of radius 2.83 ± 0.10 μm. The scattering length densities were fixed at the values quoted in Table 2, as derived from the SANS data analysis detailed below. We note in passing that the extended tail of the data at longer spin echo lengths suggests that there is in fact a dispersion in the particle sizes of the agglomerates.

No structure was observed in the pre-solvent blended sample on SESANS length scales, however some depolarisation is observed <P>=0.9953 which can be attributed to very small

structures (well below the micron level observed in the mixed powder sample). In the micrographs obtained by optical microscopy there is some evidence for larger structures in the pre-solvent blended sample. However, Figure 2(b) shows that the area ratio is one order of magnitude smaller than that of the mixed powders. The change in SESANS polarization ratio as a function of spin echo length is given by $P = P_0 \exp(\Sigma_t [G(z)-1])$, where G(z) is the projection of the density distribution along the measurement axis and the term Σ_t (the fraction of neutrons that are scattered only once) in a binary mixture scales with the volume fraction Φ as $\Phi(1-\Phi)$. Hence if one assumes that the area ratio of agglomerates measured at the surface is consistent with their volume fraction in the bulk then the change in polarisation ratio would be of the order 1%, which is at the limits of detection for the instrument used.

In order to probe the bulk nano-morphology of the composite samples at length-scales from ~1 – 200 nm, we used SANS and the results are shown in Figure 4. In SANS, the intensity is proportional to the number, size and contrast of the scattering entities in a sample, while the *q*-dependence of the intensity is related to their shape and local arrangement. So in our composites it is the scattering from the C_{60} that dominates the SANS, not the hydrogenous PS (which would be expected to contribute a mostly flat background).

We have started our analysis of the SANS data by determining if processing induces any nanoscale orientation in our samples. In the Supporting Information, Figure S.I.4.(a) shows the 2D SANS patterns from extruded ribbons processed from both a pre-solvent blend and from mixed powders, and in Figure S.I.4.(b) we show the corresponding intensity ratios $I(Q_V)/I(Q_H)$ as a function of q for the vertical and horizontal quadrants of the 2D patterns. As clearly shown, the nanoscale distribution of C_{60} aggregates in the extruded ribbons is isotropic. Accordingly, the SANS data were circularly-averaged to produce 1D graphs of intensity *vs q*.

As shown in Figure 4(a) for the pre-solvent blended composite, five different samples

were analyzed using SANS, namely: (a) a compression molded sample annealed at 90 ºC for 5 minutes; (b) a similarly compression molded sample annealed at 170 ºC for 5 minutes; (c) an extruded sample collected at P2; (d) an extruded sample collected at P9 and (e) an extruded ribbon.

As can be seen in Figure 4(a), the neutron scattering intensity *I(q)* of the compression molded sample annealed at 90 ºC for 5 minutes is very weak and only increases slightly when the annealing temperature increases to 170 ºC. Our goal on testing these samples at these two temperatures (90 ºC and 170 ºC), intermediate between room temperature and the extrusion temperature (200 ºC), was to study the effect of temperature alone on the nano-morphology of the composite samples as they are heated at the very beginning of the extruder.

(a)

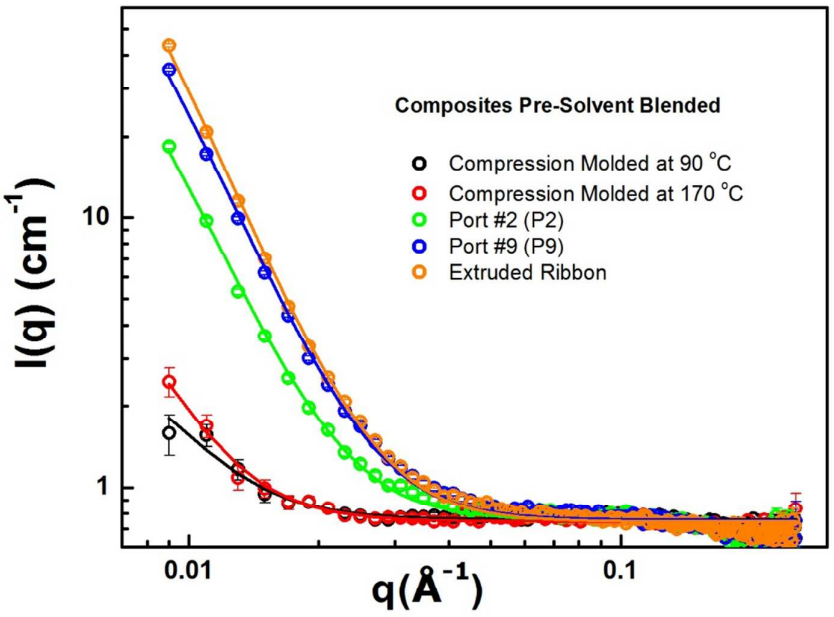

(b)

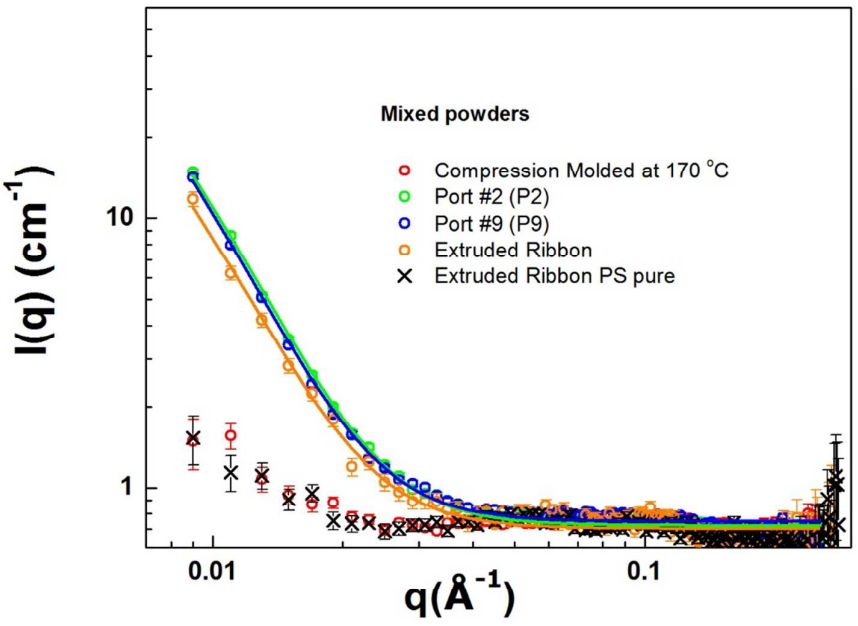

Figure 4. SANS data from extruded PS-C_{60} nanocomposites (identical scales have been used for ease of comparison): (a) Pre-solvent blended; (b) Prepared from mixed powders of PS and C_{60}.

When the composites are fed into the extruder an abrupt increase of nearly 1 order of magnitude in scattering intensity occurs in the early stages of the extrusion process, as revealed by a comparison between the two previous samples and the sample P2. Indeed, it can be seen that the scattering intensity continues to increase further along the extruder, reaching a maximum value in the extruded ribbon.

Figure 4(b) presents the SANS data for the corresponding composites prepared from mixed powders of the pure components PS and C_{60}. Also shown for comparison are the background (incoherent) SANS scattering of a ribbon of pure PS extruded under the same conditions, as well as the SANS of a sample prepared by compression molding at 170 ºC consisting of C_{60} and PS powders in the weight ratio 1:99. This sample corresponds to the unmixed reference, i.e. a sample in which C_{60} and PS are not intermixed (situation A in

Figure 1). As seen in Figure 4(b), there is again an almost 1 order of magnitude increase in scattering intensity in the early part of the extruder, i.e. from the powder mixture at the inlet (here represented by our "unmixed reference") to sampling location P2. But, contrary to what is observed with the pre-solvent blended composites, the scattering intensity changes very little with processing from sampling location P2 to the die outlet.

We continued our SANS analysis by determining the slopes of the SANS data in their linear regions (between 0.009 and 0.015 $Å^{-1}$ for the pre-solvent processed composite samples compression molded at 90 ºC and 170 ºC, and between 0.009 and 0.025 $Å^{-1}$ for the pre-solvent processed composite samples collected from the extruder and for the composite samples prepared from mixed powders) with a simple power law model fit of the form $I(q) \propto q^{-m}$, where m is related to the fractal dimension of the underlying structure.

Considering first the samples prepared from pre-solvent processed composites, we find the value of m increases from 1.2 at 90 ºC, to 1.8 at 170 ºC, and to 2.7, 3.1 and 3.3 at sampling locations P2, P9 and the extruded ribbon, respectively (see details in Table 2). This indicates that with increasing temperature and residence time inside the extruder, the mass distribution of C_{60} changes from something sparsely distributed to something more clustered, with the PS-C_{60} interfaces becoming better defined. These factors point to nano-agglomeration of the C_{60}.

Turning now to the composite samples prepared from mixed powders of PS and C_{60}, we find that the value of m exhibits a small decrease from 2.6 in P2, 2.5 in P9 and 2.4 in the extruded ribbon (Table 2). This indicates that processing induces a slight shift in the C_{60} mass distribution towards something less clustered and with more diffuse PS-C_{60} interfaces, suggesting some improvement of dispersion in these composites.

		C_{DB} (Å^{-4})	$\Delta\rho$ (Å^{-2})	Length L (nm)	m
Pre-Solvent Blended	90 ºC	$2.5 \times 10^{-6} \pm 2.9 \times 10^{-7}$	3.91×10^{-7}	14.7 ± 4.1	1.2 ± 0.3
	170 ºC	$3.9 \times 10^{-6} \pm 1.2 \times 10^{-6}$	4.88×10^{-7}	25.0 ± 12.3	1.8 ± 0.3
	P2	$3.8 \times 10^{-5} \pm 8.4 \times 10^{-7}$	1.52×10^{-6}	20.7 ± 0.8	2.7 ± 0.03
	P9	$7.3 \times 10^{-5} \pm 1.1 \times 10^{-6}$	2.11×10^{-6}	20.5 ± 0.5	3.1 ± 0.02
	Ribbon	$9.7 \times 10^{-5} \pm 2.2 \times 10^{-6}$	2.44×10^{-6}	25.5 ± 0.9	3.3 ± 0.02
From Mixed Powders	P2	$3.2 \times 10^{-5} \pm 3.8 \times 10^{-7}$	1.40×10^{-6}	14.9 ± 0.4	2.6 ± 0.03
	P9	$3.0 \times 10^{-5} \pm 3.9 \times 10^{-7}$	1.35×10^{-6}	15.6 ± 0.5	2.5 ± 0.03
	Ribbon	$2.4 \times 10^{-5} \pm 7.6 \times 10^{-7}$	1.21×10^{-6}	14.9 ± 1.2	2.4 ± 0.07

Table 2. SANS fitting parameters (DAB model) for the q range 0.009 – 0.2545 Å^{-1}. C_{DB} is the scaling factor, $\Delta\rho$ is the contrast between the two phases, L is the average distance between the two phases and m is the slope of the SANS data in their linear region extracted using the power law model ($I(q) \propto q^{-m}$).

A more quantitative approach to interpreting the SANS data is to model-fit it over its full range (q = 0.009 – 0.2545 Å^{-1}). The model we have chosen to use for this is the Debye-Bueche (DB), also called the Debye-Anderson-Brumberger (DAB), model [44, 45] (Equation 1). This model calculates the scattering from a randomly distributed, two-phase system that is characterized by a single length scale - the correlation length, L - which is a measure of the average spacing between regions of the two different phases (1 and 2). Crucially, this model makes no assumptions about the underlying morphology of the sample. The DAB function has the form

$$I(\mathrm{q}) = C_{DB}\frac{L^3}{(1+(qL)^2)^2} + background \qquad (1)$$

where the pre-factor $C_{DB} = 8\pi K(\Delta\rho)^2\phi_1\phi_2$, where $\Delta\rho$ is the neutron scattering length density

difference between the phases having volume fractions of ϕ_1 and ϕ_2 and K is a scalar to convert the units of L^{-1} to those of $I(q)$ (i.e. cm^{-1}).

As shown in Figure 4, the DAB model (solid lines) gives a good description of the data. We have not fitted the data for the sample of mixed powders compression molded at 170 ºC (sample "mixed powders – initial" in Figure S.I.2 in Supporting Information) and for the extruded ribbon of pure PS because neither of these samples conforms to the physics of the DAB model. The small amount of residual low-q scattering that is evident in these two samples results most likely from some large-scale heterogeneities (e.g., voids).

The values obtained from the fitting for C_{DB} and L using Equation 1 are shown in Table 2. The values of $\Delta\rho$ calculated from the respective C_{DB} values are also included. All these values are depicted graphically in Figure 5.

(a)

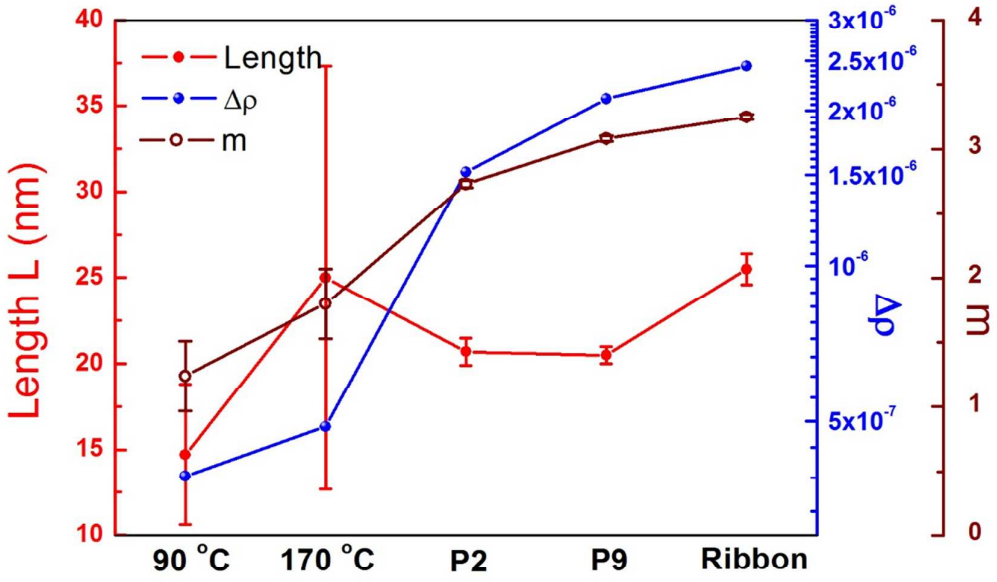

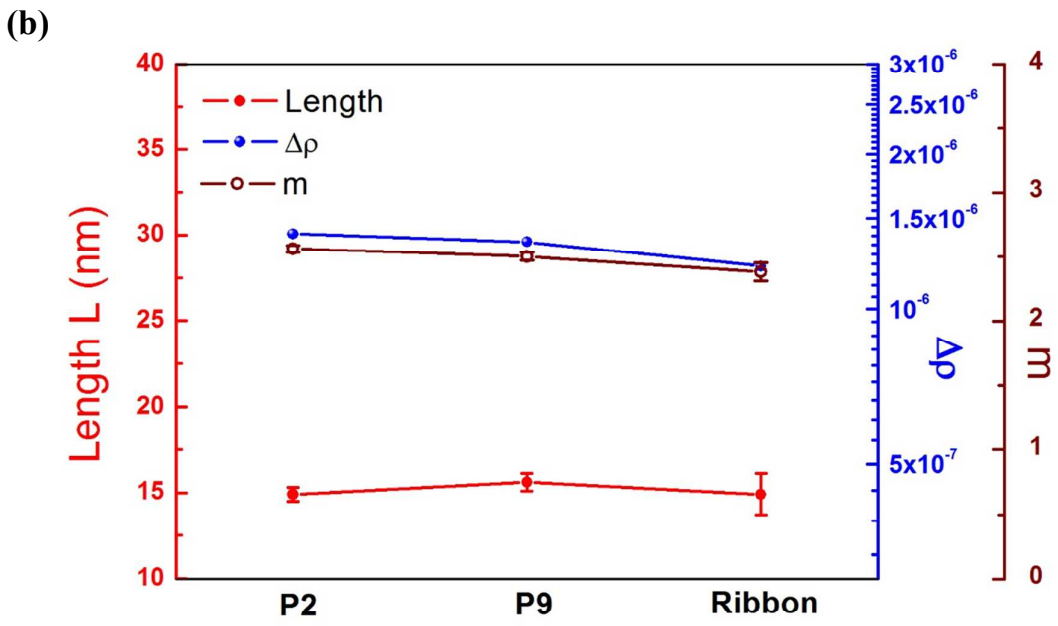

Figure 5. Evolution of the correlation length (L), phase contrast ($\Delta\rho$) and slope (m) with processing for the samples prepared: (a) From pre-solvent-blended composites; (b) From mixed powders of pure PS and pure C_{60}.

According to the values in Figure 5(a) and in Table 2, in the case of the samples prepared from solvent-processed blends, there is some increase in correlation length of the phase domains along the barrel of the extruder which indicates the occurrence of some phase domain coarsening. However, the most striking feature of these samples is the ~1 order of magnitude increase in the scattering length density difference between the two phases ($\Delta\rho$), from 3.91 x 10^{-7} Å^{-2} in the initial sample to 2.44 x 10^{-6} Å^{-2} in the extruded ribbon, which clearly indicates that during processing the phases become purer due to C_{60} re-agglomeration. In the extreme situation of having pure phases of PS and pure phases of C_{60} the corresponding $\Delta\rho$ would be 4.19 x 10^{-6} Å^{-2}.

According to Figure 5(b) and Table 2, in the case of composite samples prepared from powder mixtures of pure C_{60} and PS, the correlation length between the two phases remains

approximately constant (~15 nm) from sample P2 to the extruded ribbon and the phase contrast decreases slightly suggesting only a slight improvement in the quality of the nano-dispersion.

In summary, therefore, our SANS results show that the major changes in the nano-morphology of the PS-C_{60} composites occur in the early stages of the extrusion process, between the hopper and sampling port #2. This is in accordance with observations reported for other polymer-based systems, such as polymer blends and composites containing layered silicates, carbon nanotubes or graphene derivatives. As the material reaches the first kneading zone of the screw, it melts as a result of a combination of conducted and dissipated heat. Since melt temperatures are still low, hydrodynamic stresses are high, favouring dispersion. Moreover, flow through kneading disks is complex, promoting distribution. Furthermore, according to our SANS results, in the case of composites prepared from the pre-solvent blend the main morphological evolution that occurs along the extruder is a continuous re-agglomeration of the initially molecularly dispersed C_{60} into purer phase domains. In the case of composites prepared from mixed powders the main morphological evolution is an initial abrupt increase in the degree of dispersion up to sampling location P2, followed by a much less visible morphological evolution from P2 to the die exit.

Figure 6 illustrates the SAXS data for the same samples as in Figure 4, namely in Figure 6(a) for the pre-solvent blended composites heated to 90 ºC, 170ºC and also collected from P2, P9 and extruded ribbon, and in Figure 6(b) for the composites compounded from mixed powders and collected at P2, P9 and extruded ribbon. Again, data in the q range 0.009 – 0.025 $Å^{-1}$ was fitted with a linear power law and obtained values of m. These are plotted in Figure S.I.5. in the Supporting Information.

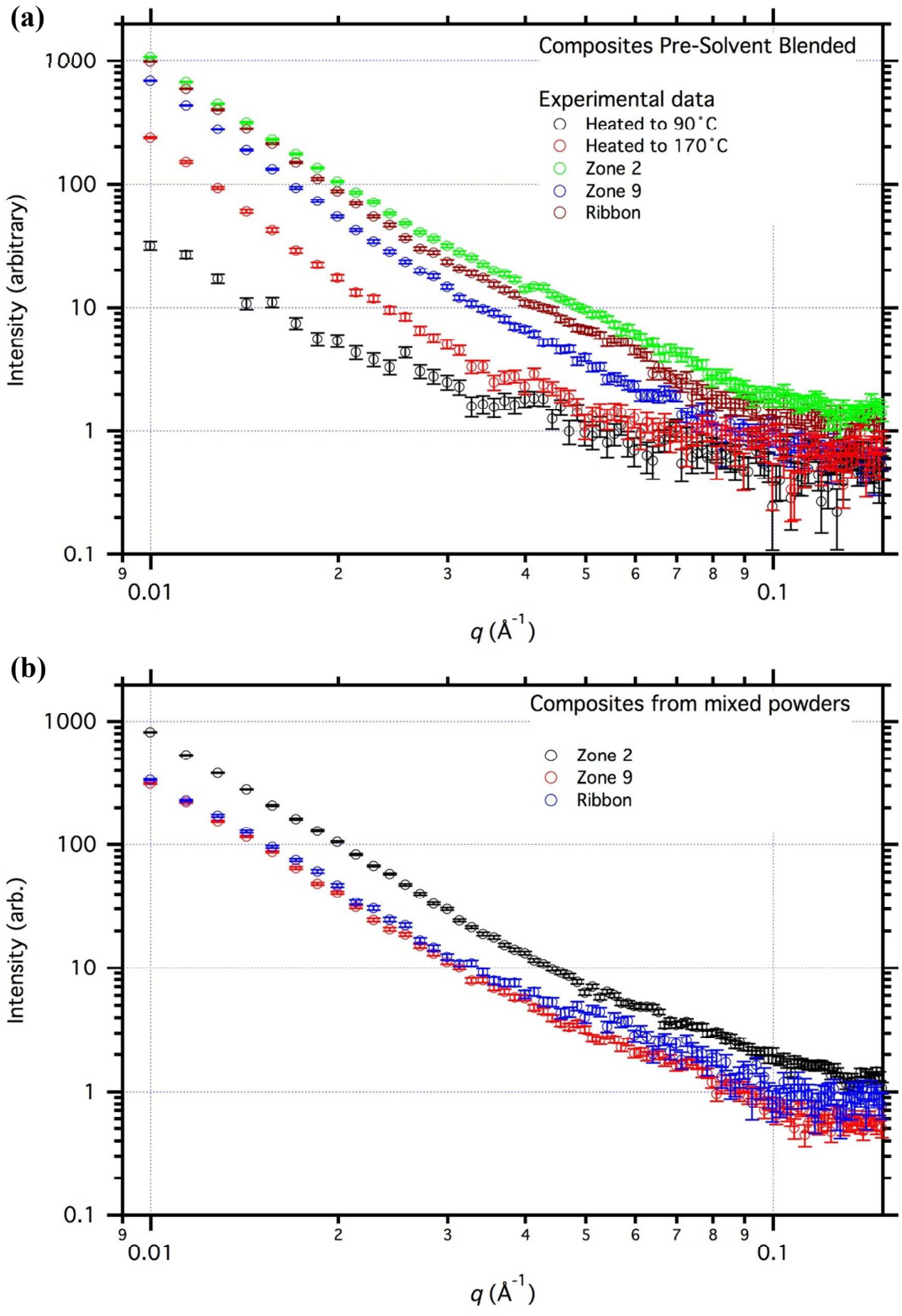

Figure 6. Small angle X-ray scattering of extruded PS and PS-C_{60} nanocomposites: (a) Pre-solvent blended; (b) Prepared from mixed powders of PS and C_{60}.

As seen, in both Figures 6(a) and 6(b) as well as in Figure S.I.5. in Supporting Information, the SAXS data show trends very similar to those observed in the corresponding SANS data, namely: (a) in the case of pre-solvent blended composites *m* increases progressively from *m*=2.5 in the sample heated to 90 ºC to *m*=3.4 in the extruded ribbon; (b) in the case of composites from mixed powders *m* changes only very little between sampling location P2 and the extruded ribbon, specifically a small decrease is observed from *m*=3.0 in location P2 to *m*=2.9 in the extruded ribbon. These observations corroborate the previous SANS results showing that: (a) in the case of samples prepared from pre-solvent processed blends, PS-C_{60} interfaces become progressively sharper as the material progresses along the screw which points strongly to the occurrence of C_{60} re-agglomeration; (b) in the case of samples prepared from mixed powders, there is a slight improvement in mixing from sampling location P2 to the extruded ribbon with the PS-C_{60} interfaces becoming slightly less sharp.

The 1D WAXS patterns for the two samples prepared from the two different feeding formulations and collected from sampling port #P9 are shown in Figure S.I.6. in Supporting Information. In both samples the two broad amorphous halos with maxima at q = 0.75 $Å^{-1}$ and q = 1.35 $Å^{-1}$ are due to the amorphous polystyrene. For mixed powders, at location P9 a crystalline C_{60} peak is clearly visible at q = 0.77 $Å^{-1}$ as well as two small peaks at q = 1.26 and 1.48 $Å^{-1}$ [34]. These peaks, which are not visible in the pre-solvent processed sample, are due to the presence of crystalline C_{60} aggregates [21, 34]. These results reinforce those obtained by O.M. and SESANS showing that extruded samples processed from mixed powders retain crystalline C_{60} aggregates while the samples processed from pre-solvent blend either do not have any crystalline C_{60} aggregates or have them in such a low quantity that they are below the detection limit of the WAXS technique.

To investigate this morphological evolution further, we have performed some

Transmission Electron Microscopy (TEM) analysis of the samples collected from P2 and P9 for both the composites prepared from mixed powders and from pre-solvent blend. Figures S.I.7 and S.I.8 in Supporting Information show some representative TEM images. The TEM images show that in the case of composites processed from mixed powders the size and number of aggregates decreases along the extruder and in the case of composites processed from the solvent blend the size and number of the aggregates increases along the extruder, a finding in good qualitative agreement with our SANS data.

Before proceeding further, we believe it is important to make a few comments about the complementarity of some of the different direct measurement techniques for assessing nanocomposite morphology. Whilst TEM is arguably more accessible than neutron scattering, it nonetheless has some drawbacks, particularly for studying polymer composites. First, there is the issue of the representative nature of the sampling process: TEM is subjective in the sense that the operator must search the sample for regions of interest, and those regions of interest must be at, or near to, the surface of the sample. In contrast SANS is a bulk sampling technique: the beam is essentially the same size as the sample and the weak neutron-nucleus interaction conveys depth penetration. In the present work we have used a 10 mm diameter neutron beam, meaning the illuminated area ~78 mm^2 (= 78,000,000 μm^2). However, in the TEM pictures shown in the Supporting Information the maximum area probed in a single picture (Figure S.I.7.(a)) is only ~60 μm^2. SAXS suffers from a similar limitation to TEM in this respect. Second, to achieve any penetration into a sample with electron or X-ray beams it is necessary to use beams of high energy (many keV), energies that are way beyond covalent bond energies meaning that there is a significant possibility of radiation-induced damage in the sample. The 'cold' neutrons used in SANS, on the other hand, have energies of just a few meV, meaning SANS is a genuinely non-destructive technique. Lastly, there is the issue of phase contrast. Electrons and X-rays interact with atomic electrons meaning that the greatest

contrast is obtained between elements of significantly different atomic number. In our samples we have carbon dispersed in a matrix of carbon and hydrogen. This means that, for example, in the TEM pictures we have provided in the Supporting Information, there is no reliable way of knowing if what we see are aggregates of C_{60} in a matrix of pure PS or regions rich in C_{60} in a soup of PS with some very well molecularly dispersed C_{60}. In SANS, however, the phase contrast also stems from the neutron-nucleus interaction and can be very different between nuclei of similar atomic number, as it indeed is between carbon and hydrogen. Thus, whilst our neutron measurements do not provide the same visually-intuitive picture of a sample that TEM does, they are sensitive to structural information that TEM simply is not.

In Figure 7 we show the DSC data, where we plot the variation of the glass transition temperature T_g with processing. The T_g of the pure polystyrene is ~102.4 ºC. In the case of composites processed from mixed powders of C_{60} and PS we observe that the corresponding T_g increases to ~103.2 ºC at location P2 and then remains approximately unaltered at P9 and in the extruded ribbon. Based on previous work [19, 32, 34] this ~0.8 ºC increase in T_g may be explained by the occurrence of some molecular dispersion of C_{60} in the PS matrix and corroborates our SANS results. It also shows that this molecular dispersion principally occurs in the first part of the extruder, i.e. between the hopper and sampling location P2. In the case of the samples extruded using pre-solvent blended composites we note that the T_g of the initial solvent blended powder was ~100ºC, i.e. lower than the T_g of the pure polymer. This most likely results from the fact that the solvent-blended composite still contained some traces of solvent trapped inside the material in spite of the drying under vacuum at 100 ºC for several hours. In order to probe for the presence of trapped-solvent we have performed some thermogravimetric analysis (TGA) of the solvent-blended composites (Figure S.I.9. in Supporting Information) which showed no clear evidence of its presence, within the

resolution of the technique. However, we did observe contamination on surface of solvent processed samples caused by the electron beam (Figure S.I.10). This well-known surface contamination is electron beam induced deposition of excess volatile carbonaceous species. These observations strongly suggest that trapped-solvent is present in very small amounts, although enough to decrease the T_g of the system by several degrees Celsius.

The most interesting feature of the T_g of the solvent-blended composites, is that it drops from ~99.7 ºC to ~96.6 ºC respectively at P2 and P9 and then it remains approximately constant between P9 and the extruded ribbon. Based also on previous work [19, 32, 34], this decrease in T_g along the extruder is most likely due to the fact that C_{60} is leaving the PS matrix and re-agglomerating, as also supported by our SANS results.

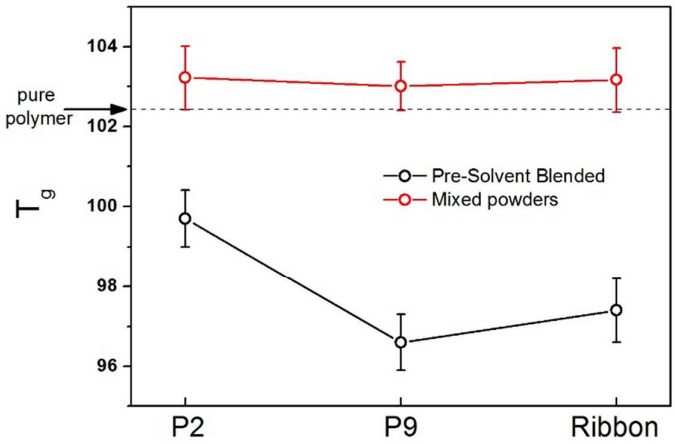

Figure 7. Variation of the glass transition temperature (T_g) along processing. T_g was determined using the extrapolated half-C_p method. Associated error bars are typically < ±1 ºC.

Figure 8 shows the mechanical spectra of the PS matrix and the composites obtained when processing the pre-solvent blended composites (a) or the mixed powders (b).

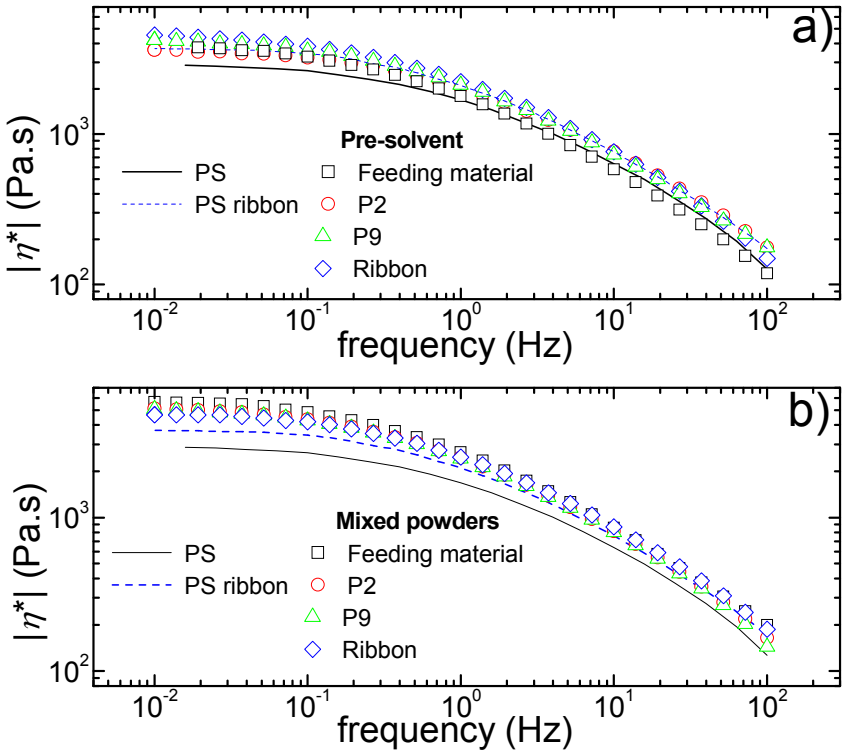

Figure 8. Frequency dependence of the dynamic viscosity |η*| for the matrix (lines), the solvent prepared composite (a) and the mixed powders composite (b) all measured at different locations along the extruder.

Rheological data of PS samples collected along the extruder first reveal that the PS matrix is sensitive to processing. The PS ribbon spectrum is shifted to larger viscosity values for all frequencies with respect to the PS powder sample. Thermo-oxidative crosslinking reported recently for a PS nanocomposite [46] could explain the increase in the zero shear viscosity of PS ribbon samples. This degradation process is further supported by the rheological data presented in Figure S.I.11. (in Supporting Information), where a gradual increase in the zero shear viscosity of PS samples collected along the extrusion line relates with the increasing residence time of each sample in the extruder.

Although entanglements in the PS matrix are evident in the master curve (see Figure S.I.12. in Supporting Information which shows a rubbery plateau prior to the glass transition regime), no reduction in the zero shear viscosity of the PS nanocomposite produced with the

solvent method is seen in Figure 8(a). Thus the non-Einstein behavior reported elsewhere for a similar system [16, 47] and for other well dispersed polymer nanocomposites [46, 48] is not reproduced here. The C_{60} dispersion quality required to produce a viscosity reduction is not met in the powder sample produced with the solvent method. Indeed SANS indicated that the minimum distance between aggregates is of the order of 15 nm in this sample, which is much larger than the size of the PS chain. This poor molecular dispersion of C_{60} therefore explains the reinforcement of the PS matrix mirrored in the enhanced viscoelasticity for all frequencies.

The melt processing of the solvent based PS composite is accompanied with an increase in the dynamic viscosity. Indeed, the progressive increase from P2 to P9 does partially correlate with the viscosity increase of the thermally degraded matrix, as demonstrated by the constant viscosity ratio between composite and matrix which nearly matches an Einstein like value between P2 and P9 (see Figure S.I.13. in Supporting Information).

However, the breakdown of Einstein like behavior for the powder sample is concomitant with the presence of structural heterogeneities below 20 nm in the solvent based PS composite which impedes the interpretation of the rheological data using classical continuum theories [11]. Overall, rheological changes along the processing of the solvent based feeding formulation are in harmony with the re-agglomeration process (SANS and TEM data both showing a coarsening of the structure along the extruder) which progressively leads to an Einstein-like reinforcement of the PS matrix.

The situation is changed for the mixed powders as the Newtonian viscosity in Figure 8(b) shows a monotonic decrease along the extruder. In contrast to this, the high frequency regime of the dynamic viscosity is not sensitive to the residence time in the extruder nor to the progressive structural rearrangement. Thus, the process-induced reduction in C_{60} aggregates size does not impact on the entanglement plateau, whereas it accelerates the terminal

relaxation time of the PS matrix. Similar effects were reported in well dispersed PS nanocomposites containing dendritic polyethylene particles [46] or PS nanoparticles [49]. Confinement of PS chain together with additional free volume brought by the nanoparticles were called for explaining the non-classical viscosity reduction in the latter system, whereas such effects were ruled out for the former polymer nanocomposite. Although local chain confinement cannot be excluded (the SANS analysis suggests an aggregate-aggregate distance of the order of 15 nm), the existence of large aggregates in microscopic imaging supports the larger viscosity and slower dynamics of the mixed powders when compared to the neat PS.

Rationalizing the zero shear viscosities of the composites and the PS matrix shows that after P9, no evolution is observed in the rheology of the processed mixed powders. This is in contrast to the viscosity increase from P9 to the extrudate observed with the solvent route, which eventually results in a close matching between the rheological properties of the two extrudates (see Figure S.I.14. in Supporting Information).

Thus, this rheological similarity suggests a dynamically equivalent macroscopic morphology for the two types of composite extrudates. However, the routes for achieving similar viscosity levels are different, as the re-agglomeration of the solvent based feeding formulation opposes to the break-up/erosion of aggregates and molecular dispersion of C_{60} in the composites from mixed powders.

The relative sizes of PS chains and aggregates, the dynamics of the polymer close to the aggregates, the interfacial tensions, the aggregates-aggregates interactions and C_{60}-PS interactions all contribute in a complex fashion to the rheology of these composites. Because the interplay between rheology and all these ingredients is far from being understood even in model systems [50], the rheological data collected in Figure 8 essentially indicate that for the

present PS-C_{60} composite, the re-agglomeration process gives way to an increase in the dynamic viscosity, whereas the structural sizing down corresponds to reduced viscosity.

4. Conclusions

In this work we studied the effect of the initial feeding formulation on the morphology evolution of PS-C_{60} nanocomposites along the axis of a twin screw extruder. Two markedly different initial feed formulations comprising 1 wt% C_{60} were used, namely: (a) a simple mechanical mixture of PS and C_{60} powders and (b) a PS-C_{60} composite prepared by solvent blending. The study was carried out by performing sequential sampling along the extruder and by characterizing the corresponding degrees of dispersion. A number of experimental techniques were used to probe the dispersion levels at different length scales, namely: optical microscopy, spin-echo small angle neutron scattering (SESANS), small angle neutron scattering (SANS), small angle x-ray scattering (SAXS) and wide-angle x-ray scattering (WAXS). These are complemented by differential scanning calorimetry (DSC) and rheological measurements.

According to our results, the vastly different morphologies of the initial feeding formulations (situation A for mixed powders and situation D for the solvent blend, in Figure 1) converge along the extruder into a similar final nanomorphology (situation C in Figure 1) which strongly suggests that the final morphology is mainly dictated by the coupling between thermodynamics and flow leading to a preferred steady state of the system which is independent of the initial conditions.

Furthermore, this work strongly suggests that starting from a perfectly solvent-blended mixed system and promoting its re-agglomeration along the extruder might be a good strategy to prepare nanocomposites when some level of particle aggregation is advantageous to specific applications [10, 11].

Acknowledgments

This work was funded by FEDER funds through the COMPETE 2020 Program and National Funds through FCT - Portuguese Foundation for Science and Technology under the project UID/CTM/50025/2013. Funding from FEDER through the program COMPETE (Project EXPL/CTM-POL/0933/2012) is also acknowledged.

SANS data were collected during beam time provided through the user program at the ISIS Neutron and Muon Source, operated by the UK Science & Technology Facilities Council.

We thank Chris Duif (TU Delft) for assistance with the SESANS measurements.

This work benefited from DANSE software developed under NSF award DMR-0520547.

Author Contributions

G.B., J.A.C. and L.H. originated the initial experimental and overall motivation for the work. L.F. prepared the solvent-blended composite. H.G. and P.T. performed the extrusion experiments. R.S. undertook the optical microscopy characterization. W.G.B. and S.R.P. conducted the Spin-Echo-SANS characterization. G.B., S.M.K., A.J.P. and N.C. performed the SANS measurements and analysis. M.W. and N.C. carried out the SAXS measurements and analysis. A.J.P. undertook the WAXS analysis. G.B and H.G. performed the DSC characterization. L.H., P.T. and H.G. performed the rheological characterization. C.J.H. undertook the TEM analysis. K.J.A. carried out the STEM characterization. G.B. performed the TGA study. G.B. wrote the initial draft of the manuscript with inputs from all the authors and subsequently the draft was revised by all the authors.

References

1. Verdejo, R.; Bernal, M. M.; Romasanta, L. J.; Lopez-Manchado, M. A. Graphene filled polymer nanocomposites. *Journal of Materials Chemistry* **2011,** 21 (10), 3301-3310

2. Cai, D.; Song, M. Recent advance in functionalized graphene/polymer nanocomposites. *Journal of Materials Chemistry* **2010,** 20 (37), 7906-7915

3. Sahoo, N. G.; Rana, S.; Cho, J. W.; Li, L.; Chan, S. H. Polymer nanocomposites based on functionalized carbon nanotubes. *Progress in Polymer Science* **2010,** 35 (7), 837-867

4. Karatrantos, A.; Composto, R. J.; Winey, K. I.; Clarke, N. Structure and Conformations of Polymer/SWCNT Nanocomposites. *Macromolecules* **2011,** 44 (24), 9830-9838

5. Tung, W. S.; Bird, V.; Composto, R. J.; Clarke, N.; Winey, K. I. Polymer Chain Conformations in CNT/PS Nanocomposites from Small Angle Neutron Scattering. *Macromolecules* **2013,** 46 (13), 5345-5354

6. Tung, W. S.; Composto, R. J.; Clarke, N.; Winey, K. I. Anisotropic Polymer Conformations in Aligned SWCNT/PS Nanocomposites. *Acs Macro Letters* **2015,** 4 (9), 916-920

7. Kota, A. K.; Cipriano, B. H.; Duesterberg, M. K.; Gershon, A. L.; Powell, D.; Raghavan, S. R.; Bruck, H. A. Electrical and rheological percolation in polystyrene/MWCNT nanocomposites. *Macromolecules* **2007,** 40 (20), 7400-7406

8. Badamshina, E.; Gafurova, M. Polymeric nanocomposites containing non-covalently bonded fullerene C-60: properties and applications. *Journal of Materials Chemistry* **2012,** 22 (19), 9427-9438

9. Karatrantos, A.; Clarke, N.; Kröger, M. Modeling of Polymer Structure and Conformations in Polymer Nanocomposites from Atomistic to Mesoscale: A Review. *Polymer Reviews* **2016,** 56 (3), 385-428

10. Balazs, A. C.; Emrick, T.; Russell, T. P. Nanoparticle polymer composites: Where two small worlds meet. *Science* **2006,** 314 (5802), 1107-1110

11. Jancar, J.; Douglas, J. F.; Starr, F. W.; Kumar, S. K.; Cassagnau, P.; Lesser, A. J.; Sternstein, S. S.; Buehler, M. J. Current issues in research on structure-property relationships in polymer nanocomposites. *Polymer* **2010,** 51 (15), 3321-3343

12. Scurati, A.; Feke, D. L.; Manas-Zloczower, I. Analysis of the kinetics of agglomerate erosion in simple shear flows. *Chemical Engineering Science* **2005,** 60 (23), 6564-6573

13. Domingues, N.; Gaspar-Cunha, A.; Covas, J. A.; Camesasca, M.; Kaufman, M.; Manas-Zloczower, I. Dynamics of Filler Size and Spatial Distribution in a Plasticating Single Screw Extruder - Modeling and Experimental Observations. *International Polymer Processing* **2010,** 25 (3), 188-198

14. Hedberg, K.; Hedberg, L.; Bethune, D. S.; Brown, C. A.; Dorn, H. C.; Johnson, R. D.; Devries, M. Bond Lengths in Free Molecules of Buckminsterfullerene, C60, From Gas-Phase Electron-Diffraction. *Science* **1991,** 254 (5030), 410-412

15. Mu, M.; Seitz, M. E.; Clarke, N.; Composto, R. J.; Winey, K. I. Polymer Tracer Diffusion Exhibits a Minimum in Nanocomposites Containing Spherical Nanoparticles. *Macromolecules* **2011,** 44 (2), 191-193

16. Tuteja, A.; Duxbury, P. M.; Mackay, M. E. Multifunctional nanocomposites with reduced viscosity. *Macromolecules* **2007,** 40 (26), 9427-9434

17. Kropka, J. M.; Sakai, V. G.; Green, P. F. Local polymer dynamics in polymer-C-60 mixtures. *Nano Letters* **2008,** 8 (4), 1061-1065

18. Vogiatzis, G. G.; Theodorou, D. N. Local Segmental Dynamics and Stresses in Polystyrene-C-60 Mixtures. *Macromolecules* **2014,** 47 (1), 387-404

19. Wong, H. C.; Sanz, A.; Douglas, J. F.; Cabral, J. T. Glass formation and stability of polystyrene-fullerene nanocomposites. *Journal of Molecular Liquids* **2010,** 153 (1), 79-87

20. Bernardo, G.; Deb, N.; King, S. M.; Bucknall, D. G. Phase behavior of blends of PCBM with amorphous polymers with different aromaticity. *Journal of Polymer Science Part B: Polymer Physics* **2016,** 54 (10), 994-1001

21. Campbell, K.; Gurun, B.; Sumpter, B. G.; Thio, Y. S.; Bucknall, D. G. Role of Conformation in pi-pi Interactions and Polymer/Fullerene Miscibility. *Journal of Physical Chemistry B* **2011,** 115 (29), 8989-8995

22. Perrin, L.; Nourdine, A.; Planes, E.; Carrot, C.; Alberola, N.; Flandin, L. Fullerene-based processable polymers as plausible acceptors in photovoltaic applications. *Journal of Polymer Science Part B-Polymer Physics* **2013,** 51 (4), 291-302

23. Chakraborty, C.; Malik, S.; Guenet, J.-M. Syndiotactic Polystyrene/Fullerene Composites: Elucidation of Structural Aspect. *Polymer-Solvent Complexes and Intercalates - Polysolvat 8* **2011,** 303

24. Troitskii, B. B.; Troitskaya, L. S.; Dmitriev, A. A.; Yakhnov, A. S. Inhibition of thermo-oxidative degradation of poly(methyl methacrylate) and polystyrene by C60. *European Polymer Journal* **2000,** 36 (5), 1073-1084

25. Zeinalov, E. B.; Kossmehl, G. Fullerene C-60 as an antioxidant for polymers. *Polymer Degradation and Stability* **2001,** 71 (2), 197-202

26. Fernandes, L.; Gaspar, H.; Bernardo, G. Inhibition of thermal degradation of polystyrene by C-60 and PCBM: A comparative study. *Polymer Testing* **2014,** 40, 63-69

27. Pereira, P.; Gaspar, H.; Fernandes, L.; Bernardo, G. Impact of fullerenes on the thermal stability of melt processed polystyrene and poly(methyl methacrylate) composites. *Polymer Testing* **2015,** 47, 130-136

28. Higuchi, A.; Agatsuma, T.; Uemiya, S.; Kojima, T.; Mizoguchi, K.; Pinnau, I.; Nagai, K.; Freeman, B. D. Preparation and gas permeation of immobilized fullerene membranes. *Journal of Applied Polymer Science* **2000,** 77 (3), 529-537

29. Hanson, B.; Pryamitsyn, V.; Ganesan, V. Computer Simulations of Gas Diffusion in Polystyrene-C-60 Fullerene Nanocomposites Using Trajectory Extending Kinetic Monte Carlo Method. *Journal of Physical Chemistry B* **2012,** 116 (1), 95-103

30. Han, J. T.; Lee, G.-W.; Kim, S.; Lee, H.-J.; douglas, J. F.; Karim, A. Direct observation of interfacial C-60 cluster formation in polystyrene-C-60 nanocomposite films. *Nanotechnology* **2009,** 20 (10), 105705

31. Alekseeva, O. V.; Barannikov, V. P.; Bagrovskaya, N. A.; Noskov, A. V. DSC investigation of the polystyrene films filled with fullerene. *Journal of Thermal Analysis and Calorimetry* **2012,** 109 (2), 1033-1038

32. Weng, D.; Lee, H. K.; Levon, K.; Mao, J.; Scrivens, W. A.; Stephens, E. B.; Tour, J. M. The influence of Buckminsterfullerenes and their derivatives on polymer properties. *European Polymer Journal* **1999,** 35 (5), 867-878

33. Dattani, R.; Cabral, J. T. Polymer fullerene solution phase behaviour and film formation pathways. *Soft Matter* **2015,** 11 (16), 3125-3131

34. Sanz, A.; Wong, H. C.; Nedoma, A. J.; Douglas, J. F.; Cabral, J. T. Influence of C-60 fullerenes on the glass formation of polystyrene. *Polymer* **2015,** 68, 47-56

35. Rekveldt, M. T.; Plomp, J.; Bouwman, W. G.; Kraan, W. H.; Grigoriev, S.; Blaauw, M. Spin-echo small angle neutron scattering in Delft. *Review of Scientific Instruments* **2005,** 76 (3), 033901

36. Londono, J. D.; Narten, A. H.; Wignall, G. D.; Honnell, K. G.; Hsieh, E. T.; Johnson, T. W.; Bates, F. S. Composition Dependence of the Interaction Parameter in Isotopic Polymer Blends. *Macromolecules* **1994,** 27 (10), 2864-2871

37. Novais, R. M.; Covas, J. A.; Paiva, M. C. The effect of flow type and chemical functionalization on the dispersion of carbon nanofiber agglomerates in polypropylene. *Composites Part a-Applied Science and Manufacturing* **2012,** 43 (6), 833-841

38. Machado, A. V.; Covas, J. A.; van Duin, M. Evolution of morphology and of chemical conversion along the screw in a corotating twin-screw extruder. *Journal of Applied Polymer Science* **1999,** 71 (1), 135-141

39. Akeroyd, F.; Ansell, S.; Antony, S.; Arnold, O.; Bekasovs, A.; Bilheux, J.; Borreguero, J.; Brown, K.; Buts, A.; Campbell, S.; Champion, D.; Chapon, L.; Clarke, M.; Cottrell, S.; Dalgliesh, R.; Dillow, D.; Doucet, M.; Draper, N.; Fowler, R.; Gigg, M. A.; Granroth, G.; Hagen, M.; Heller, W.; Hillier, A.; Howells, S.; Jackson, S.; Kachere, D.; Koennecke, M.; Le Bourlot, C.; Leal, R.; Lynch, V.; Manuel, P.; Markvardsen, A.; McGreevy, R.; Mikkelson, D.; Mikkelson, R.; Miller, R.; Nagella, S.; Nielsen, T.; Palmen, K.; Parker, P. G.; Pascal, M.; Passos, G.; Perring, T.; Peterson, P. F.; Pratt, F.; Proffen, T.; Radaelli, P.; Rainey, J.; Ren, S.; Reuter, M.; Sastry, L.; Savici, A.; Taylor, J.; Taylor, R. J.; Thomas, M.; Tolchenov, R.; Whitley, R.; Whitty, M.; Williams, S.; Zhou, W.; Zikovsky, J. Mantid: Manipulation and Analysis Toolkit for Instrument Data. http://dx.doi.org/10.5286/SOFTWARE/MANTID (Date of access: 20/07/2016),

40. Alina, G.; Butler, P.; Cho, J.; Doucet, M.; Kienzle, P. SasView. http://www.sasview.org/ (Date of access: 20/07/2016),

41. Alig, I.; Poetschke, P.; Lellinger, D.; Skipa, T.; Pegel, S.; Kasaliwal, G. R.; Villmow, T. Establishment, morphology and properties of carbon nanotube networks in polymer melts. *Polymer* **2012,** 53 (1), 4-28

42. Vilaverde, C.; Santos, R. M.; Paiva, M. C.; Covas, J. A. Dispersion and re-agglomeration of graphite nanoplates in polypropylene melts under controlled flow conditions. *Composites Part a-Applied Science and Manufacturing* **2015,** 78, 143-151

43. Andersson, R.; van Heijkamp, L. F.; de Schepper, I. M.; Bouwman, W. G. Analysis of spin-echo small-angle neutron scattering measurements. *Journal of Applied Crystallography* **2008,** 41 (5), 868-885

44. Debye, P.; Bueche, A. M. Scattering by an Inhomogeneous Solid. *Journal of Applied Physics* **1949,** 20 (6), 518-525

45. Debye, P.; Anderson, H. R.; Brumberger, H. Scattering by an Inhomogeneous Solid .2. The Correlation Function and its Application. *Journal of Applied Physics* **1957,** 28 (6), 679-683

46. Goldansaz, H.; Goharpey, F.; Afshar-Taromi, F.; Kim, I.; Stadler, F. J.; van Ruymbeke, E.; Karimkhani, V. Anomalous Rheological Behavior of Dendritic Nanoparticle/Linear Polymer Nanocomposites. *Macromolecules* **2015,** 48 (10), 3368-3375

47. Mackay, M. E.; Dao, T. T.; Tuteja, A.; Ho, D. L.; Van Horn, B.; Kim, H. C.; Hawker, C. J. Nanoscale effects leading to non-Einstein-like decrease in viscosity. *Nature Materials* **2003,** 2 (11), 762-766

48. Nusser, K.; Schneider, G. J.; Pyckhout-Hintzen, W.; Richter, D. Viscosity Decrease and Reinforcement in Polymer-Silsesquioxane Composites. *Macromolecules* **2011,** 44 (19), 7820-7830

49. Tuteja, A.; Mackay, M. E.; Hawker, C. J.; Van Horn, B. Effect of ideal, organic nanoparticles on the flow properties of linear polymers: Non-Einstein-like behavior. *Macromolecules* **2005,** 38 (19), 8000-8011

50. Song, Y.; Zheng, Q. Linear rheology of nanofilled polymers. *Journal of Rheology* **2015,** 59 (1), 155-191

A Journey Along the Extruder with Polystyrene:C_{60} Nanocomposites: Convergence of Feeding Formulations into a Similar Nano-Morphology

Hugo Gaspar, Paulo Teixeira, Raquel Santos, Liliana Fernandes, Loic Hilliou, Michael P. Weir, Andrew J. Parnell, Kerry J. Abrams, Christopher J. Hill, Wim G. Bouwman, Steven R. Parnell, Stephen M. King, Nigel Clarke, José A. Covas, Gabriel Bernardo